A physics-informed neural network for interpretable membrane-fouling prediction with adaptive transitions between fouling mechanisms

Citation for the original published paper (version of record):
Saeedi Garakani, S., Hassanabadi, M., Chew, J. (2026). A physics-informed neural network for interpretable membrane-fouling prediction with adaptive transitions between fouling mechanisms. Separation and Purification Technology, 394(Part 2). http://dx.doi.org/10.1016/j.seppur.2026.137512

Separation and Purification Technology 394 (2026) 137512

Contents lists available at ScienceDirect

Separation and Purification Technology

journal homepage: www.elsevier.com/locate/seppur

A physics-informed neural network for interpretable membrane-fouling prediction with adaptive transitions between fouling mechanisms

Sadaf Saeedi Garakani [a], Majid Hassanabadi [b], Jia Wei Chew [a,*]

[a] Department of Chemistry and Chemical Engineering, Chalmers University of Technology, Gothenburg, Sweden
[b] Department of Computer and Systems Sciences, Stockholm University, Stockholm, Sweden

ARTICLE INFO

Keywords:
Separation
Membrane fouling
Flux decline
Mechanistic interpretability
Machine learning

ABSTRACT

Membrane fouling remains a major challenge in filtration processes, causing flux decline, reduced efficiency, and higher operational costs. Classical models such as the Hermia blocking laws describe idealized single fouling mechanisms but fail to capture the complex, dynamic transitions that occur in practical systems. Combined or empirical models offer more realism but often suffer from non-unique parameter fitting and limited interpretability, reducing their predictive reliability. Recent advances in machine learning (ML) have improved predictive accuracy, yet purely data-driven approaches lack physical grounding and require extensive datasets. To bridge this gap, we propose a Physics-Informed Neural Network (PINN) that integrates the four classical Hermia fouling mechanisms – complete pore blockage, intermediate blockage, pore constriction, and cake filtration - within a single, physically constrained data-driven model. The PINN employs adaptive sigmoid weighting functions for smooth and continuous transitions between filtration stages, and a probabilistic loss formulation that balances data fidelity, physical constraints, and initial conditions through adaptive weights. Validated on a diverse dataset encompassing multiple membrane types, transmembrane pressures, and feed conditions, the model identifies stage transitions between dominant fouling mechanisms and quantifies the relative contribution of each fouling mechanism. The developed PINN achieves high predictive accuracy with low uncertainty, outperforming classical fouling models while offering mechanistic interpretability and a physically consistent basis for membrane-fouling prediction.

1. Introduction

Membrane technology has emerged as a cornerstone of modern separation processes, offering distinct advantages such as low energy requirement, continuous operation, and high selectivity based on properties like size, charge, and chemical affinity [1]. Its versatility has led to widespread adoption across industries ranging from water and wastewater treatment to bioprocessing, food, and gas separation, highlighting its transformative potential. However, the persistent challenge of membrane fouling (i.e., the accumulation of particles, microorganisms, and organic matter on or within the membrane) continues to hinder large-scale implementation by reducing permeate flux, degrading performance, and increasing operational costs [2]. Notably, fouling-related costs have been reported to contribute substantially to operating expenditures, with estimates of approximately 20–30% in membrane-based water treatment systems [3,4]. Consequently, enhancing understanding and predictive capability of the fouling phenomena and robust strategies for their mitigation remains essential for optimizing membrane-based processes [5].

Membrane fouling is a multifaceted phenomenon driven by several interacting mechanisms, including complete and intermediate pore blocking, pore constriction, and cake-layer formation, each contributing differently to flux decline [6]. Classical empirical and semi-empirical models, such as Hermia's laws and the critical-flux hypothesis, attempt to describe these mechanisms through mathematical formulations. While these models provide useful insights, they often oversimplify the dynamic interplay and transitions among fouling mechanisms in practice (e.g., a shift from pore-blocking-dominated behavior in early filtration to cake-filtration dominance at later stages), resulting in limited predictive capability and suboptimal process control [7]. To address these shortcomings, combined fouling models have been proposed. For instance, Ho and Zydney [8] integrated pore blocking and cake filtration for BSA fouling, Duclos-Orsello et al. [9] combined pore constriction, complete pore blocking, and cake filtration, Trinh et al.

* Corresponding author.
E-mail address: jia.chew@chalmers.se (J.W. Chew).

https://doi.org/10.1016/j.seppur.2026.137512
Received 24 November 2025; Received in revised form 4 March 2026; Accepted 5 March 2026
Available online 6 March 2026

[10] coupled internal cake formation with pore constriction and pore blockage, and Zydney [11] described interconnected pore structures with permeable foulant layers. Although these approaches incorporate greater physical realism, they typically demand intensive mathematical treatment, detailed system characterization, and rely on restrictive assumptions, which limit their general applicability. Furthermore, they often rely on multi-parameter fitting in which different parameter sets can reproduce similar flux-decline trajectories, resulting in parameter non-uniqueness, and thus limiting the interpretability and transferability of fitted parameters across operating conditions.

With the advent of machine learning (ML), new opportunities have emerged for modeling complex membrane-fouling dynamics. Representative models include feedforward neural networks (NNs), support vector machines (SVM), ensemble tree-based methods such as random forests (RF) and gradient boosting (e.g., XGBoost), and deep-learning architectures designed for sequential filtration data, such as long short-term memory (LSTM) and gated recurrent units (GRU) [12–14]. Liu et al. [15] [16] demonstrated that neural networks can outperform single Hermia block-law models by capturing nonlinear, time-dependent fouling behavior across diverse microfiltration conditions, while Tanudjaja et al. [17] used random forests on decades of protein-fouling data to identify pore size as a dominant driver of flux and rejection. Additional studies using statistical methods, genetic algorithms, and hybrid frameworks further enhance predictive and optimization capabilities [18–20]. Comparative work shows that ANNs generally improve predictive accuracy over Hermia models, whereas genetic programming can provide explicit, interpretable relationships [21], and reviews highlight the effectiveness of ANNs, SVMs, and GAs for fouling prediction [22]. SVM classifiers have also been used for mechanism identification, distinguishing fouling behaviors induced by different biopolymer/EPS surrogates [23]. Despite these advances, purely data-driven models often require large datasets and remain difficult to interpret physically, limiting explainability and robustness. To overcome these limitations, recent research has shifted toward hybrid or "grey-box" models, which integrate machine learning with physical principles. This emerging field of physics-informed machine learning (PIML) incorporates governing equations via partial differential equations (PDEs) into the learning framework to ensure that predictions remain consistent with known physical laws. The seminal paper by Raissi et al. [24] conceptualized physics-informed neural networks (PINNs), i.e., NNs trained not only to fit experimental data but also to satisfy governing physical equations through physics-based loss terms, by embedding the Navier-Stokes equations within deep-learning architectures, achieving both high accuracy and physical consistency in fluid mechanics. Similarly, Tagliavini et al. [25] combined fluorescence spectroscopy with mechanistic modeling and ML to enhance ultrafiltration flux predictions, demonstrating the benefit of integrating physical constraints for meaningful parameter estimation. Such physics-aware or grey-box models improve both generalization and interpretability, bridging the gap between data-driven prediction and physical understanding. Despite these advances, a persistent limitation is the lack of a unified, physically consistent framework that can simultaneously represent mixed fouling mechanisms, quantify their time-varying contributions, and identify transition times during filtration.

Building upon this progress, our previous study introduced a PINN framework that embedded Hermia's fouling laws into a neural-network architecture, enabling mechanistically sound and data-efficient fouling modeling [26]. The model successfully identified dominant fouling mechanisms and achieved accurate predictions using only 20% of the available data for training, demonstrating its efficiency and interpretability. In the present study, we advance this approach by developing an enhanced PINN framework that dynamically learns fouling kinetics, assigns fractional weights to each fouling mechanism over time, and automatically determines transition points between fouling stages. Importantly, integrating all four Hermia mechanisms within a single unified framework enables the model to capture mixed and evolving fouling behavior without manual mechanism selection or switching between mechanisms, while providing an interpretable, time-resolved decomposition of the contribution of each mechanism to flux decline. This new framework provides a continuous and physically consistent representation of fouling evolution throughout filtration. By coupling adaptive sigmoid-based regime transitions with learned loss weighting, the model achieves both high predictive accuracy and mechanistic transparency. This innovation represents a significant step toward data-efficient, interpretable, and generalizable models for membrane fouling prediction and process optimization.

Reported PINNs applications in membrane fouling modeling have largely focused on physically consistent prediction and/or inference of effective parameters, typically demonstrated on specific systems and operating conditions. The framework proposed here extends this concept by introducing a unified physics-informed representation of multiple fouling mechanisms within a single PINN architecture. By simultaneously embedding the four Hermia blocking laws and enabling smooth, learnable transitions between them, the model can dynamically capture evolving fouling stages without manual mechanism selection. In addition to predicting flux decline, the framework quantifies the time-resolved contribution of each fouling mechanism and identifies transition times between stages, providing a mechanistically interpretable representation of multi-stage fouling dynamics.

2. Methods

2.1. Governing equations

The fouling models proposed by Hermia over four decades ago [7] remain a foundational framework for describing the inevitable flux decline observed in membrane filtration. Fig. 1 schematically illustrates the four principal fouling mechanisms, namely, complete pore blockage (i.e., full obstruction of pore entry), intermediate pore blockage (i.e., partial blockage of pore entrance), pore constriction (i.e., reduction in pore volume due to internal fouling), and cake filtration (i.e., formation of a surface layer that adds resistance to permeation). Collectively, these mechanisms account for the characteristic decline in permeate flux over time, as expressed by the Hermia model:

$$\frac{d^2t}{dV^2} = k\left(\frac{dt}{dV}\right)^n \tag{1}$$

where V is the cumulative permeate volume over filtration time t. The corresponding form in terms of permeate flux J is:

$$\frac{dJ}{dt} = -k_n J^{3-n} \tag{2}$$

where k_n is the permeability parameter, and n is a characteristic exponent specific to each fouling mechanism.

Understanding the dominance and interaction of these mechanisms is essential, as fouling remains a major constraint in membrane-based separations. Each mechanism affects performance differently and dictates appropriate cleaning strategies. In practice, fouling rarely occurs through a single mechanism acting alone; instead, multiple mechanisms

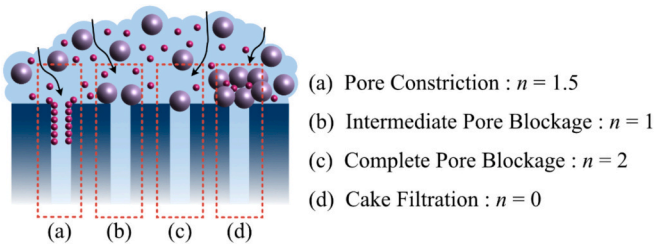

Fig. 1. Schematic diagram of the four basic membrane-fouling mechanisms.

often operate concurrently. To capture these dynamics, several combined or composite models have been developed that integrate two or more fouling mechanisms [27,28]. While such models advance conceptual understanding, their application can be challenging, especially under conditions of steep initial flux decline. Moreover, parameters derived from these models typically indicate only the relative dominance of each mechanism between cases, rather than providing a quantitative measure of their contributions throughout the flux decline. Addressing this limitation forms the focus of the present work.

2.2. Physics-informed neural network architecture

A fully connected feedforward Physics-Informed Neural Network (PINN) was developed to model membrane fouling dynamics, using the Hermia fouling laws as the governing physical constraints (Fig. 2). The network comprises an input layer, two hidden layers of 300 neurons each employing hyperbolic tangent (tanh) activation functions, and a single-neuron linear output layer predicting the permeate flux $J(t)$ as a function of normalized time t (scaled from the physical time domain [0, t_{max}] to [0,1]). The architecture and training hyperparameters (tanh activation, Adam optimizer, learning rate 0.001) were chosen based on our previous study [26], which demonstrated stable and accurate convergence for similar membrane-fouling PINN formulations. The same hyperparameter settings were applied across all datasets and operating conditions considered in this study; no case-specific tuning (e.g., grid search) was performed, and dropout was not used.

The fouling rate coefficients, k_n, for each regime were treated as learnable parameters. To ensure physical plausibility (i.e., $k_n > 0$), the unconstrained scalar parameters were transformed via the softplus function. The fixed exponents, $n = 2, 1.5, 1, \text{or } 0$, correspond to the four classical fouling mechanisms defined by Hermia's model (Fig. 1).

To capture smooth transitions between fouling regimes, three trainable transition parameters (namely, $t_{\text{transition1}}$, $t_{\text{transition2}}$, and $t_{\text{transition3}}$) were introduced along the normalized time axis. These transition times are learned from unconstrained trainable variables and mapped into the interval $[0, 1]$ using sigmoid functions. Sigmoid functions are chosen because they enable smooth, differentiable transitions between fouling regimes, avoiding discontinuities associated with abrupt switching and supporting stable gradient-based training. Successive transitions accumulate through additional sigmoid-scaled delta (Δ) parameters, producing piecewise-weighted contributions from each fouling residual. This formulation enables the model to represent gradual mechanism shifts while maintaining differentiability throughout, ensuring stable and efficient backpropagation during training.

Consequently, the flux decline curve is divided into four distinct stages – labelled I, II, III, and IV in Fig. 2 - each corresponding to a dominant fouling mechanism or combination of mechanisms. The framework assumes that flux decline under the studied conditions can be represented by the four classical Hermia fouling mechanisms, with the overall filtration trajectory described through stage-wise evolution and smooth transitions. Effects not explicitly modeled by Hermia's formulation (e.g., detailed transport or hydrodynamic phenomena) are implicitly captured through the learned kinetics and stage-wise weighting. Overall, this formulation enables the network to combine data fidelity with physically consistent structure, bridging mechanistic interpretability and predictive accuracy for membrane-fouling prediction.

2.3. Physics-informed loss formulation

For each of the four stages in the flux decline curve (i.e., I, II, III, and IV in Fig. 2), Hermia's law is consistently imposed as the governing physical constraint:

$$\frac{dJ}{dt} + k_n |J|^{3-n} = 0 \tag{3}$$

The first derivative, $\frac{dJ}{dt}$, is obtained through automatic differentiation of the PINN output with respect to the normalized time t. To represent different fouling behaviors, four residuals – corresponding to each fouling mechanism - are formulated and then combined using differentiable indicator functions.

To delineate the four consecutive fouling stages, three transition time parameters – $t_{transition1}$, $t_{transition2}$, $t_{transition3}$ - are defined along the normalized time axis. Each is treated as an unconstrained variable during optimization and mapped to the interval [0,1] using a standard

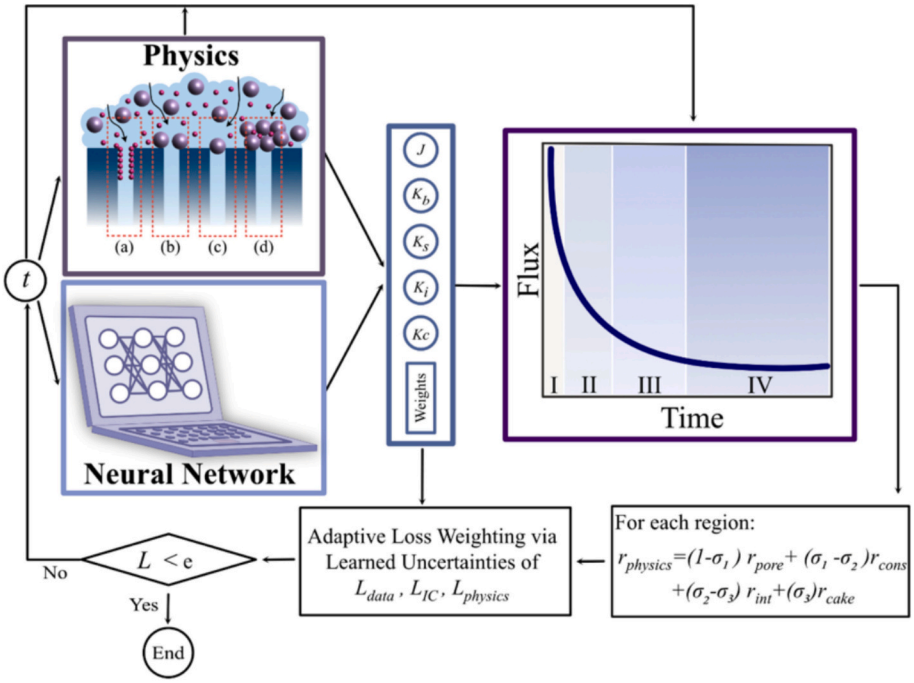

Fig. 2. Architecture of physics-informed neural network (PINN).

sigmoid function:

$$t_{eff} = \sigma\left(t_{unconstrained}\right) \tag{4}$$

To enforce an ordered progression of $0 < t_{transition1} < t_{transition2} < t_{transition3} < 1$, two additional unconstrained Δ parameters are introduced and mapped using sigmoid functions, such that each subsequent transition is defined as a positive fraction of the remaining time interval, ensuring a physically consistent sequence of transitions. Specifically, the effective ordered transition times are defined as:

$$t_{\mathrm{eff},1} = \sigma\left(t_{\mathrm{unconstrained},1}\right), t_{\mathrm{eff},2} = t_{\mathrm{eff},1} + \left(1 - t_{\mathrm{eff},1}\right)\sigma(\Delta_2), t_{\mathrm{eff},3} = t_{\mathrm{eff},2} + \left(1 - t_{\mathrm{eff},2}\right)\sigma(\Delta_3),$$

where $t_{\mathrm{unconstrained},1}$, Δ_2, and Δ_3 are unconstrained trainable scalars and $\sigma(\cdot)$ denotes the sigmoid function. This mapping guarantees $0 < t_{\mathrm{eff},1} < t_{\mathrm{eff},2} < t_{\mathrm{eff},3} < 1$ without requiring additional constraints during optimization. The resulting $t_{\mathrm{eff},i}$ are used in Eq. (5) to define the sigmoid gating functions.

To avoid discontinuities at regime boundaries, sigmoid gating functions are used to create smooth connections between adjacent residuals. The sharpness factor (set to 20) produces a steep but continuous transition, promoting numerical stability during training:

$$\sigma_i(t) = \sigma\left(20\left(t - t_{eff,i}\right)\right) \tag{5}$$

Using this formulation, the four residuals corresponding to the four fouling mechanisms are merged into a single composite residual:

$$r_{physics} = (1-\sigma_1)r_{pore-constrict} + (\sigma_1-\sigma_2)r_{intermediate-block} + (\sigma_2-\sigma_3)r_{complete-block} + (\sigma_3)r_{cake} \tag{6}$$

The mechanism weights are explicitly constrained to be nonnegative and to sum to one at each time. The physics-based loss is then defined as the mean squared value of this composite residual across all N_c collocation points $\{t_i\}$:

$$L_{physics} = \frac{1}{N_c}\sum_{i=1}^{N_c}\left[r_{physics}\left(t_i\right)\right]^2 \tag{7}$$

By embedding the governing differential equations directly into the loss function, the PINN inherently adheres to the underlying fouling dynamics. This physics-informed constraint steers the model toward physically consistent flux trajectories, enhancing both reliability and robustness. Such physics-based grey-box models provide a key advantage over purely data-driven black-box approaches by ensuring consistency with established physical laws throughout training.

2.4. Data loss and initial-condition enforcement

The experimental flux data, $J_{true}(t)$, were imported and cast into floating-point arrays. The time variables are min-max normalized to the interval [0,1], while the permeate flux was used as is and retained their original physical units. The data-fitting loss was defined as

$$L_{data} = \frac{1}{N_d}\sum_{i=1}^{N_d}\left[J(t_i) - J_{true}(t_i)\right]^2 \tag{8}$$

where N_d is the number of experimental training points.

To ensure consistency with the initial flux at $t = 0$, an additional initial-condition (IC) loss term is introduced:

$$L_{IC} = \left[J(0) - J_{true}(0)\right]^2 \tag{9}$$

The IC loss term acts as a regularization constraint, anchoring the predicted flux to the experimental value at the start of the filtration (i.e., $t = 0$) and preventing unphysical deviations during training.

Within this PINN framework, the total loss function achieves a balanced objective: (i) the data loss enforces agreement with experimental observations, (ii) the physics-based loss constrains the model to obey the governing physical laws, and (iii) the IC loss maintains adherence to the starting permeate flux. Together, these components enable the network to learn flux-decline dynamics while enforcing both data fidelity (i.e., agreement between predicted and measured data) and consistency with the governing fouling physics.

2.5. Adaptive loss weighting via learned uncertainties

To achieve balanced optimization among the different loss components, three trainable log-variance parameters are introduced: $\log\sigma_{data}$, $\log\sigma_{physics}$, and $\log\sigma_{IC}$. The total loss function is then formulated as:

$$L = e^{-\log\sigma_{data}}L_{data} + \log\sigma_{data} + e^{-\log\sigma_{physics}}L_{physics} + \log\sigma_{physics} + e^{-\log\sigma_{IC}}L_{IC} + \log\sigma_{IC} \tag{10}$$

This probabilistic weighting framework [29] allows the model to learn the relative importance of each loss term by interpreting the variance parameters as measures of uncertainty. Each component is scaled inversely to its learned uncertainty, enabling the network to adaptively balance between data fidelity, physical consistency, and boundary enforcement without manual tuning of weight coefficients.

As a result, the model can down-weight noisy experimental data or stiff physical residuals when necessary, improving training stability, convergence efficiency, and overall robustness of the PINN.

3. Results and discussion

Developing predictive models for membrane-filtration processes is a major research focus, because such models are vital for forecasting membrane system performance. Accurate prediction not only facilitates efficient process design and scale-up, but also provides critical insights into membrane fouling, one of the most persistent challenges in membrane-based operations [30].

Among the different modeling approaches, blocking laws have long served as a cornerstone for interpreting fouling behavior. Initially introduced by Hermans and Bredee [31] and later refined by Hermia [32], these models provide a mechanistic framework for describing different fouling mechanisms, including those relevant to non-Newtonian fluids (Table 1). Rooted in physical principles, blocking laws combine theoretical formulations with practical understanding of membrane operation, offering a structured means to relate permeate flux decline to underlying fouling dynamics.

Despite their strong theoretical basis, classical blocking models exhibit several limitations. Their implementation often requires extensive process characterization and detailed membrane property data, which are rarely available in practice. Furthermore, their reliance on simplifying assumptions restricts their applicability to specific operating conditions and narrow process ranges [33]. Notably, these existing models do not provide a direct means to quantify how strongly each fouling mechanism contributes to the observed flux decline. These

Table 1
Mathematical formulation of the four basic membrane-fouling mechanisms.

Fouling mechanism	n	k	Flux formulation	Eq. (#)
Cake filtration	0	k_c	$\frac{1}{J^2} = \frac{1}{J_0^2} + K_c t$	(11)
Intermediate pore blockage	1	k_i	$\frac{1}{J} = \frac{1}{J_0} + K_i t$	(12)
Pore constriction	1.5	k_s	$\frac{1}{J^{0.5}} = \frac{1}{J_0^{0.5}} + K_s t$	(13)
Complete pore blockage	2	k_b	$\ln(J) = \ln(J_0) - k_b t$	(14)
Combined: Complete Pore Blocking and Cake Filtration [8]	0 and 2	α β	$\frac{J}{J_0} = \exp(-\alpha J_0 t) + \frac{1-\exp(-\alpha J_0 t)}{\sqrt{1+\beta J_0 t}}$	(15)

Table 2
Summary of foulant and operating parameters from earlier microfiltration studies [34,35].

Case no.	Foulant	Membrane material	Pore size (μm)	TMP (bar)	Feed flow rate (L/h)	Concentration (mg/L)
1.	Laundry waste	Cellulose ester	0.22	0.5	80	Not specified
2.	Laundry waste	Cellulose ester	0.22	1.5	80	Not specified
3.	Laundry waste	Cellulose ester	0.22	0.5	60	Not specified
4.	Laundry waste	Cellulose ester	0.22	1.0	60	Not specified
5.	Laundry waste	Cellulose ester	0.22	0.5	44	Not specified
6.	Laundry waste	Cellulose ester	0.22	0.5	30	Not specified
7.	Polyamide	Cellulose acetate	5	0.3	Not specified	5
8.	Polyamide	Cellulose acetate	5	0.3	Not specified	20
9.	Polystyrene	Cellulose acetate	5	0.3	Not specified	5
10.	Polystyrene	Cellulose acetate	5	0.3	Not specified	20

constraints highlight the need for more flexible, data-informed frameworks capable of capturing the complex and dynamic nature of membrane fouling.

To evaluate the generalizability and robustness of the proposed PINN model, 20 datasets (150–350 data points each) were curated from two microfiltration studies [26,29]. The observational data are used to enforce the data-fidelity term in the composite loss function, while Hermia's fouling laws are enforced through the physics-residual loss. Accordingly, a conventional random train/validation/test split within each dataset was not applied; instead, all available points are used as data-driven constraints, and robustness is assessed by examining performance consistency across the 20 distinct experimental cases. These datasets encompass a broad spectrum of membrane-filtration scenarios, including variations in membrane type, transmembrane pressure (TMP), feed flow rate, foulant type, and foulant concentration (Table 2). For some cases, certain operating parameters (e.g., feed flow rate or concentration) were not reported in the original studies from which the datasets were compiled; these values are therefore unavailable in Table 2. Incorporating such diversity in the training data provides a rigorous assessment of the model's ability to capture distinct physical behaviors across heterogeneous systems. Although the number of experimental cases is modest compared to black-box machine-learning benchmarks, the physics-governed constraint substantially reduces the effective degrees of freedom and mitigates overfitting. Consistent with our previous PINN study, where predictive accuracy remained stable even when the available training data were reduced by 80%, this physics-regularized structure supports reliable learning and generalization under limited-data conditions [26].

Fig. 3 compares the experimental permeate flux data with predictions from the classical Hermia fouling models and the PINN model. Across all cases, no single fouling mechanism successfully reproduces both the rapid initial flux decline and the gradual long-term reduction. On the one hand, the complete pore blockage model aligns closely with the experimental data during the early stage of filtration but significantly underestimates flux once the normalized time (t) is approximately 0.1. On the other hand, the cake-filtration model provides a superior fit in the later stages but overestimates flux at the beginning. The intermediate-blocking and pore-constriction models exhibit behaviors between these extremes yet fail to accurately capture the flux evolution accurately throughout the entire filtration period.

These results confirm, expectedly, that membrane-filtration performance cannot be fully represented by any single idealized mechanism within the Hermia framework. Rather, membrane-fouling is inherently a multi-stage process, characterized generally by a transition from initial dominance of complete pore blockage to a later prevalence of cake filtration. This dynamic interplay among fouling mechanisms highlights the necessity of modeling frameworks, such as the PINN model developed here, that can adaptively track fouling mechanism transitions and thereby provide more accurate and physically consistent predictions of flux decline behavior in membrane systems.

Several researchers have proposed combined fouling models that account for the simultaneous influence of multiple fouling mechanisms. The seminal work by Ho and Zydney [8] (Eq. 15) incorporated both complete pore blocking and cake filtration into a unified framework, aiming to improve predictions of flux-decline behavior in membrane-filtration systems. Despite its conceptual appeal, the practical application of this model presents challenges. Effective use requires fitting experimental data to the proposed equation and determining two empirical parameters, namely, the pore-blockage parameter (α) and cake filtration parameter (β), which represent the relative contributions of the fouling mechanisms. However, a well-acknowledged limitation for this and similar combined fouling models [9,10] is the non-uniqueness of parameter estimation. Multiple distinct values of α can yield similarly high coefficients of determination (R^2), indicating equally good fits to the experimental data. As shown in Table 3, α values differing by orders of magnitude yield similar MSE and R^2 values. This lack of parameter uniqueness undermines confidence in such models' ability to capture the true underlying fouling dynamics and, consequently, to reliably predict membrane-filtration performance. When different combinations of α and β can explain the flux-decline data equally well, it becomes difficult to draw physically meaningful conclusions about the dominant fouling mechanisms under specific operating conditions. Thus, while combined models offer a more comprehensive theoretical representation of fouling behavior, their heavy reliance on empirical parameter fitting - in the absence of physical constraints - introduces uncertainty that limits their interpretability and practical utility.

Given the challenges associated with accurate physical descriptions of flux-decline trends, more advanced modeling frameworks are necessary. Machine learning offers a powerful means of representing the complexity and nonlinearity inherent in membrane fouling. To address this gap, our primary objective is to develop a data-driven model constrained by physical governing equations, thereby providing a dynamic and interpretable representation of fouling behavior throughout the filtration process.

Membrane filtration generally exhibits a sequential flux-decline profile: an initial phase dominated by pore blockage, followed by a rapid decline due to pore constriction and adsorption, and finally stabilization as a cake layer forms [36,37]. Since the dominant mechanism evolves over time, a multi-stage conceptual model is needed, ideally one that can (1) identify the prevailing fouling mechanism at any given moment, and (2) determine the timing of transitions between successive mechanisms. To this end, the developed PINN framework systematically integrates the four classical Hermia fouling models as foundational components that vary in influence across filtration stages. By partitioning the flux-time trajectory into multiple, potentially unequal segments, the PINN model dynamically assigns adaptive weights to each fouling mechanism at different points in time. This approach not only enhances understanding of membrane fouling but also provides practical insights for membrane design, process optimization, and

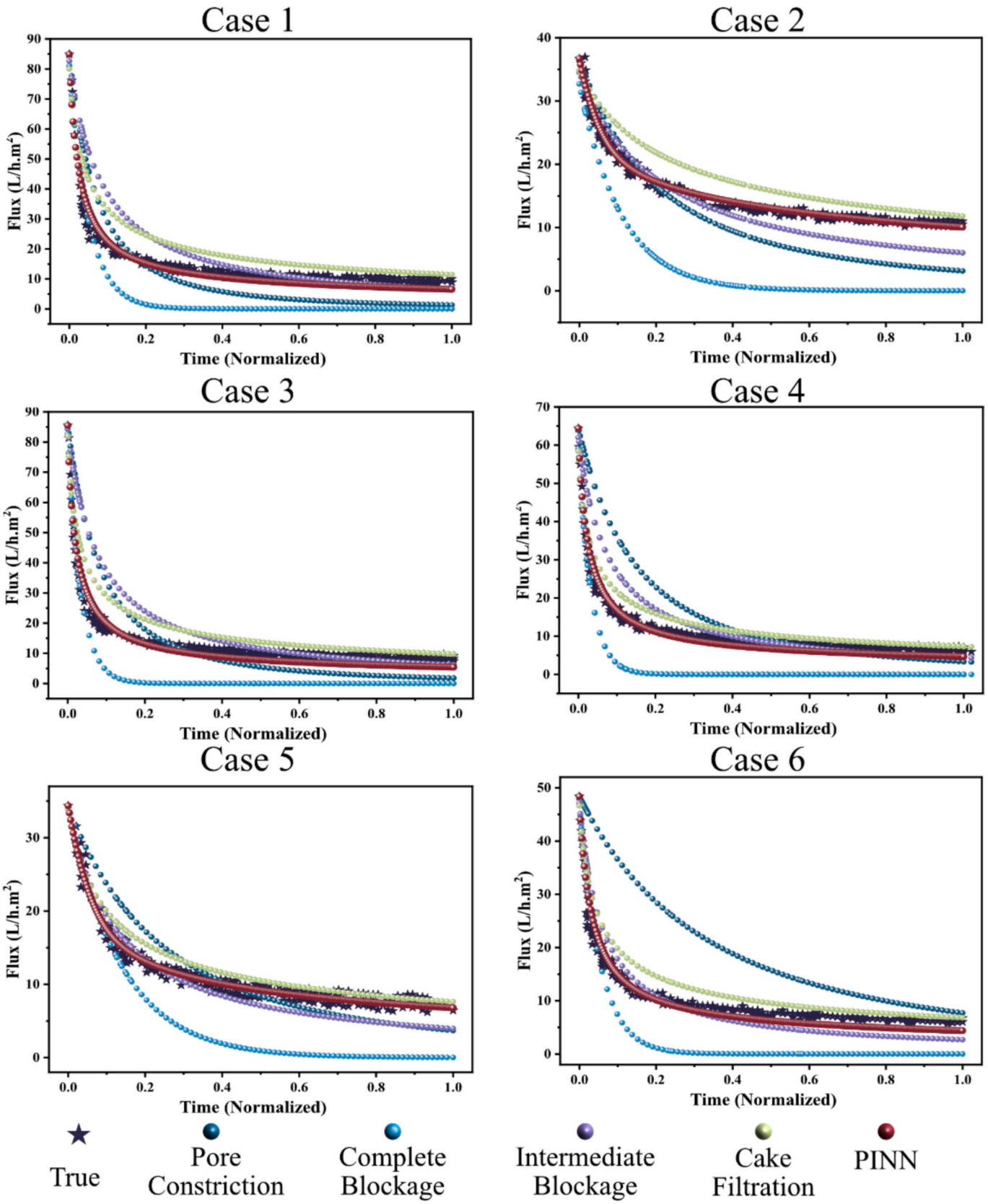

Fig. 3. Actual flux-decline trends for the 6 cases and the predicted flux based on Hermia models.

Table 3
Non-Unique fitting results to combined fouling model [8]: α values differing by orders of magnitude yielding comparable MSE and R^2.

Case no.	α	β	MSE	R^2
Case 1	0.00021	0.00059	0.00065	0.95
Case 1	0.0012	0.00059	0.0013	0.92
Case 5	0.00054	0.00023	0.0019	0.93
Case 5	6.158	0.00023	0.0024	0.91
Case 6	0.00023	0.00054	0.00206	0.93
Case 6	14.3845	0.00054	0.00155	0.95

maintenance scheduling. In particular, it enables operators to predict and plan cleaning interventions precisely when needed, tailored to the dominant fouling mechanism, thereby extending membrane lifespan, reducing operating costs, and improving overall reliability.

A further advantage of the proposed PINN is its ability to estimate transition times between consecutive stages, pinpointing when the dominance of one fouling mechanism shifts to another. This yields a temporally resolved map of fouling behavior, with precise quantification of mechanistic contributions and transitions throughout the filtration. By combining physical interpretability with predictive accuracy, the framework offers unprecedented insights into when and how specific fouling mechanisms evolve, directly informing strategies for optimal cleaning and operation. Ultimately, this physics-governed, data-driven approach bridges the gap between mechanistic modeling and real-world variability, providing a robust and generalizable tool for diagnosing, predicting, and optimizing membrane-filtration performance.

As depicted in Fig. 4 (and Figs. S1 – S11), the flux predictions generated by the PINN model exhibit excellent agreement with experimental data across ten diverse case studies. The predicted flux curves, together with variability bands obtained from multiple independent PINN trainings with different random initializations, closely follow the measured data through the entire filtration durations. The consistently high accuracy and low uncertainty demonstrate that the PINN model developed is stable, robust, and reliable, even when applied across different membrane types and operating conditions.

Table 4 and Table S1 summarize representative membrane-filtration cases analyzed using the developed PINN model. The R^2 values are consistently above 0.9, indicating good agreement between predicted and measured flux decline. For each case, the flux-time curve is partitioned into four distinct stages, with the model assigning dynamic weights to the four classical Hermia fouling mechanisms in each stage to quantify their relative contributions to the flux decline. The identified transition times ($t_{normalized}$) correspond to when the dominant fouling mechanism changes, signaling the onset of a new stage. The weights are reported to four decimal places. Values of 0.0000 or 1.0000 indicate that the underlying weight is very close to 0 or 1 at the reported precision; these do not result from a hard 0/1 constraint, but arise naturally from saturation of the sigmoid-based transition formulation (Eq. 5). To illustrate how adaptive weighting and stage transitions are inferred, Case 7 is described here as an example. In Stages I and II ($t < t_2$), complete pore blockage is the most dominant followed by pore constriction, consistent with a rapid initial flux decline. As filtration progresses into Stage III, pore constriction becomes increasingly dominant, indicating progressive internal restriction of flow paths. Finally, in Stage IV ($t \geq t_3$), cake filtration dominates with weights approaching unity, suggesting that fouling is primarily governed by deposition onto an established surface cake. Overall, this example demonstrates how the PINN provides a time-resolved mechanistic map of fouling evolution. While the inferred mechanism weights provide mechanistically interpretable insights, independent experimental characterization of foulant structures or membrane surfaces would provide valuable complementary validation of the predicted mechanism transitions.

Generally, complete pore blockage predominates at the start of filtration, then eventually giving way to cake filtration with time. A clear contrast is observed between laundry waste (Cases 1, 3, and 5) and plastic particles (Cases 7 and 10) feeds. For the latter, pore constriction becomes a significant mechanism in the intermediate stages, whereas this behavior is absent in the laundry waste cases. Among the laundry waste cases (Cases 1, 3, and 5), a lower crossflow feed rate appears to delay the onset of cake-filtration dominance, suggesting a slower accumulation of surface-deposited foulants.

In Stage I (typically within the first 0.1% and up to 5% of the filtration duration), fouling is dominated by complete pore blockage across all cases. For laundry waste (Cases 1, 3, and 5), cake filtration emerges as the secondary mechanism, while pore constriction and intermediate pore blockage remain negligible. In contrast, in plastic particle systems (Cases 7, 10), the second most dominant mechanism is pore constriction. Regarding Stage II, the dominant mechanism in Stage I gradually declines, while the secondary mechanism gains prominence. During Stage III, the secondary mechanism in Stage I generally becomes dominant. Finally, in Stage IV, cake filtration overwhelmingly dominates (with weights approaching 1), indicating that the membrane surface is largely covered by a foulant cake layer, and further fouling arises primarily from deposition onto the existing cake rather than from pore-scale effects.

These findings demonstrate that the PINN model effectively distinguishes among concurrent fouling mechanisms, accurately identifies transition points between fouling mechanisms, and quantitatively evaluates their relative dominance over time. Such mechanistic insights are critical for improving both the understanding and prediction of membrane-filtration performance, thereby informing design optimization, operation strategies, and fouling mitigation approaches. These mechanism-resolved outputs are directly actionable for membrane operation. When pore blocking dominates in early stages, mitigation can prioritize pretreatment or strategies that reduce pore-scale deposition (e.g., feed conditioning or optimized initial flux). When pore constriction emerges in intermediate stages, it may indicate a higher risk of irreversible internal fouling, motivating earlier intervention or more intensive cleaning protocols. In contrast, when cake filtration becomes dominant, operational strategies such as crossflow enhancement, backwashing, or surface-focused cleaning become more effective. Moreover, the predicted transition times provide quantitative guidance on when to intervene (e.g., scheduling cleaning before the onset of cake-dominated Stage IV), facilitating reduced downtime and improved membrane lifespan.

Fig. 5 illustrates the fouling behavior predicted by the PINN for Case 3 using two model configurations: one incorporating all four fouling mechanisms (i.e., complete pore blockage, pore constriction, intermediate pore blockage, and cake filtration) across four stages (Figs. 5a-b), and a simplified one including only two mechanisms (i.e., complete pore blockage and cake filtration) across two stages (Figs. 5c-d). Comparing Figs. 5a and c indicate that the four-mechanism model reproduces the measured flux more accurately, underscoring the need for factoring in all four mechanisms rather than the two to three in the combined models. In the corresponding fractional weight plots, Fig. 5b shows that, in the intermediate stages, multiple fouling mechanisms are

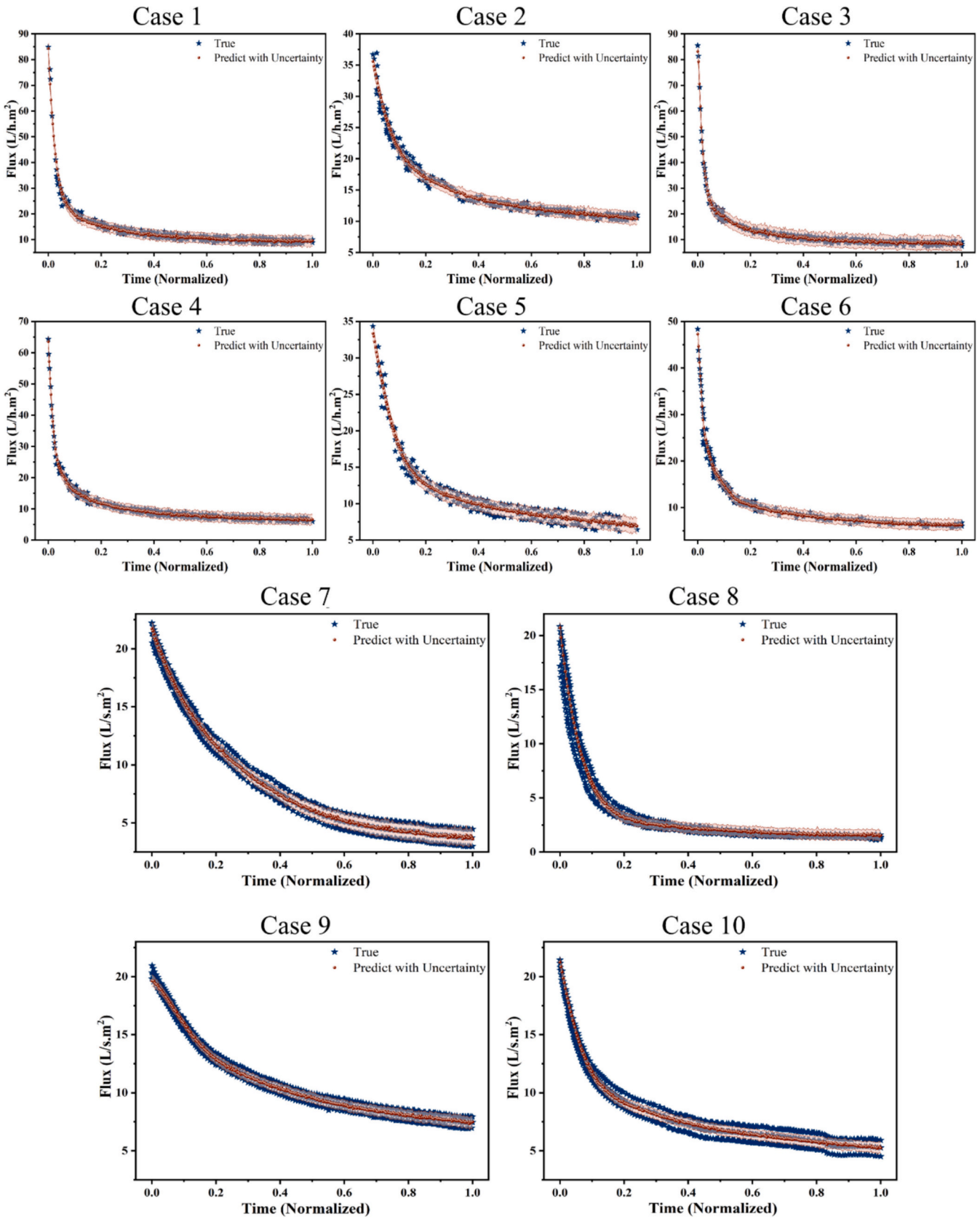

Fig. 4. Comparison of experimental flux-decline data ("True") and PINN-predicted trends (mean ± 1 standard deviation) for ten representative filtration cases. The uncertainty band is computed from multiple independent PINN trainings with different random initializations (all other settings held constant).

Table 4
Representative cases showing fouling mechanism weights and stage transitions predicted by the Physics-Informed Neural Network (PINN). Green cells denote the dominant fouling mechanism in each stage.

Case	Stage and transition time	Weight of Complete pore blockage (−)	Weight of Pore constriction (−)	Weight of Intermediate pore Blockage (−)	Weight of Cake filtration (−)
Case 1 (laundry waste) $R^2 = 0.92$	Stage I $t = 0$	0.5087	0.0243	0.0652	0.4017
	Stage II $t_1 = 0.03$	0.4927	0.0244	0.0657	0.4172
	Stage III $t_2 = 0.08$	0.4097	0.0238	0.0661	0.5004
	Stage IV $t_3 = 0.21$	0.0000	0.0000	0.0000	1.0000
Case 3 (laundry waste) $R^2 = 0.97$	Stage I $t = 0$	0.5216	0.0429	0.0460	0.3895
	Stage II $t_1 = 0.06$	0.5056	0.0431	0.0465	0.4048
	Stage III $t_2 = 0.15$	0.4223	0.0427	0.0474	0.4876
	Stage IV $t_3 = 0.24$	0.018	0.00	0.00	0.982
Case 5 (laundry waste) $R^2 = 0.97$	Stage I $t = 0$	0.5397	0.0596	0.1182	0.2826
	Stage II $t_1 = 0.0093$	0.5238	0.0601	0.1205	0.2957
	Stage III $t_2 = 0.022$	0.4401	0.0605	0.1293	0.3701
	Stage IV $t_3 = 0.049$	0.00	0.00	0.00	0.9999
Case 7 (polyamide) $R^2 = 0.91$	Stage I $t = 0$	0.5001	0.4372	0.0593	0.0034
	Stage II $t_1 = 0.013$	0.4841	0.4493	0.0629	0.0037
	Stage III $t_2 = 0.137$	0.4014	0.5079	0.0856	0.0051
	Stage IV $t_3 = 0.285$	0.0000	0.0005	0.0088	0.9907
Case 10 (polystyrene) $R^2 = 0.93$	Stage I $t = 0$	0.4954	0.3792	0.1113	0.0142
	Stage II $t_1 = 0.04$	0.4794	0.3880	0.1175	0.0151
	Stage III $t_2 = 0.099$	0.3969	0.4268	0.1553	0.0210
	Stage IV $t_3 = 0.214$	0.0000	0.0002	0.0020	0.9978

concurrently operative and transition gradually. On the other hand, when only two mechanisms are considered, Fig. 5d reveals an abrupt transition between them approximately midway through the filtration process.

From a physical standpoint, the intermediate fouling mechanisms – pore constriction and intermediate pore blockage - represent transitional processes that occur between the initial complete pore-blocking phase and the eventual cake-layer formation. Incorporating these additional mechanisms allows the PINN to more accurately describe the continuous evolution of fouling behavior that governs the experimental flux data. In contrast, excluding them forces the model to approximate intermediate behaviors with an unrealistic binary transition, thereby diminishing both the fit quality and the mechanistic interpretability of the results. From an operational perspective, the time-resolved weights derived from the four-mechanism, four-stages model provide actionable insights, indicating when pore-scale mitigation strategies are most effective and when cake-removal interventions become necessary.

Fig. 6 illustrates the fouling behavior predicted by the PINN for two particulate foulant feeds, namely, PA and PS. The analysis considers the effects of foulant concentration and the particle-to-pore size ratio (d_p/d_m; namely, 8 for PA and 22 for PS). As shown in Figs. 6a and b, regardless of PA or PS, the transition to cake filtration occurs earlier when the foulant concentration increases, indicating that higher concentrations accelerate the onset of cake formation. Furthermore, a larger d_p/d_m (as in the PS feeds) also leads to a faster transition to cake-filtration. Figs. 6c and d illustrate the fractional contribution of the cake-filtration mechanism in respectively Stages I and IV. In Stage I, cake filtration is negligible for the PA feeds, whereas cake filtration is already clearly operative for the PS feeds. The results confirm that observation confirms that higher d_p/d_m value and higher feed concentration both promote an earlier onset of the cake-filtration mechanism.

The strength of the PINN framework developed here lies in its synergistic integration of physical modeling and data-driven learning. Unlike conventional neural networks that function as data-driven "black-box" predictors, PINN directly embeds the governing equations of the classical Hermia fouling models into the learning process. This integration ensures that the model's outputs are not only consistent with experimental data, but also physically interpretable and mechanistically grounded.

A key innovation here is the incorporation of adaptive, smooth stage transitions implemented through sigmoid weighting functions. Rather than switching abruptly from one fouling stage to another, which can create unrealistic discontinuities absent in real filtration systems, the PINN allows each stage to evolve gradually depending on the relative influence of the fouling mechanisms. The significance of this design is evident in Fig. 7, where abrupt transitions between stages yield sharp drops in flux and discontinuous profiles that fail to reflect realistic membrane-filtration dynamics. Such abrupt shifts cause poor agreement between predicted and experimental data, highlighting the importance of implementing smooth stage transitions. When the stage transitions

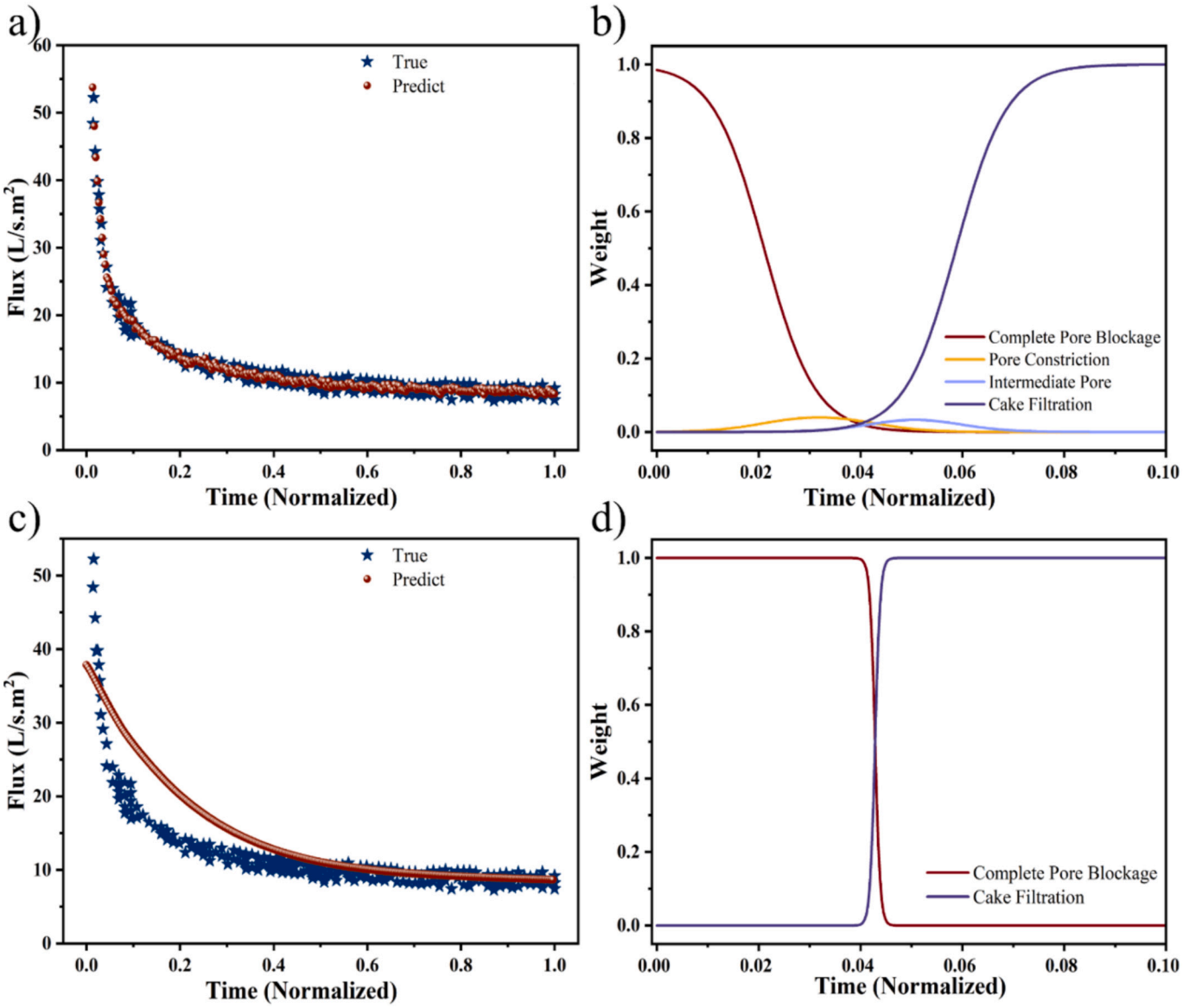

Fig. 5. (a, c) Comparison of experimental (Case 3) and PINN-predicted flux-decline curves, and (b, d) corresponding fouling-mechanism fractional weights with normalized time. Top: four-mechanisms, four-stages model; bottom: two-mechanisms, two-stages model.

are modeled using smooth sigmoid weighting functions, as shown in Fig. 4, the model captures a continuous and expected flux decline, where fouling mechanisms overlap and transition progressively. This smooth behavior aligns with the physical reality of membrane fouling, in which multiple mechanisms coexist and interact. Consequently, the comparison between Figs. 4 and 7 demonstrates that smooth transitions are essential - not only for maintaining physical consistency, but also for achieving accurate, stable, and interpretable flux predictions within the PINN framework.

Furthermore, the PINN model's loss formulation goes beyond data-fitting alone. The total loss function comprises three components: (1) the data loss, representing the difference between predicted and measured flux; (2) the physics loss, enforcing the Hermia-based differential equations that enforce the governing fouling dynamics; and (3) the initial-condition loss, which anchors the flux at the start of the filtration. Each of these losses is assigned an adaptive weight, allowing the model to autonomously balance the influence of data fidelity, physical constraints and initial conditions. This adaptive weighting eliminates the need for manual tuning and enables the network to achieve lower and more consistent prediction errors, maintaining data consistency while preserving physical integrity and reducing overall model uncertainty.

4. Conclusion

In this study, we developed a physics-informed neural network (PINN) framework for understanding and predicting membrane fouling dynamics during microfiltration. Beyond improving predictive accuracy, the proposed framework introduces a unified physics-aware representation of mixed fouling mechanisms with learnable stage transitions and mechanism-resolved temporal weighting, enabling simultaneous prediction and mechanistic interpretation of fouling evolution. Traditional mechanistic models, such as the Hermia blocking laws, are limited by their assumption of a single dominant fouling mechanism and inability to represent the gradual, overlapping transitions observed in practical membrane operations. Similarly, combined

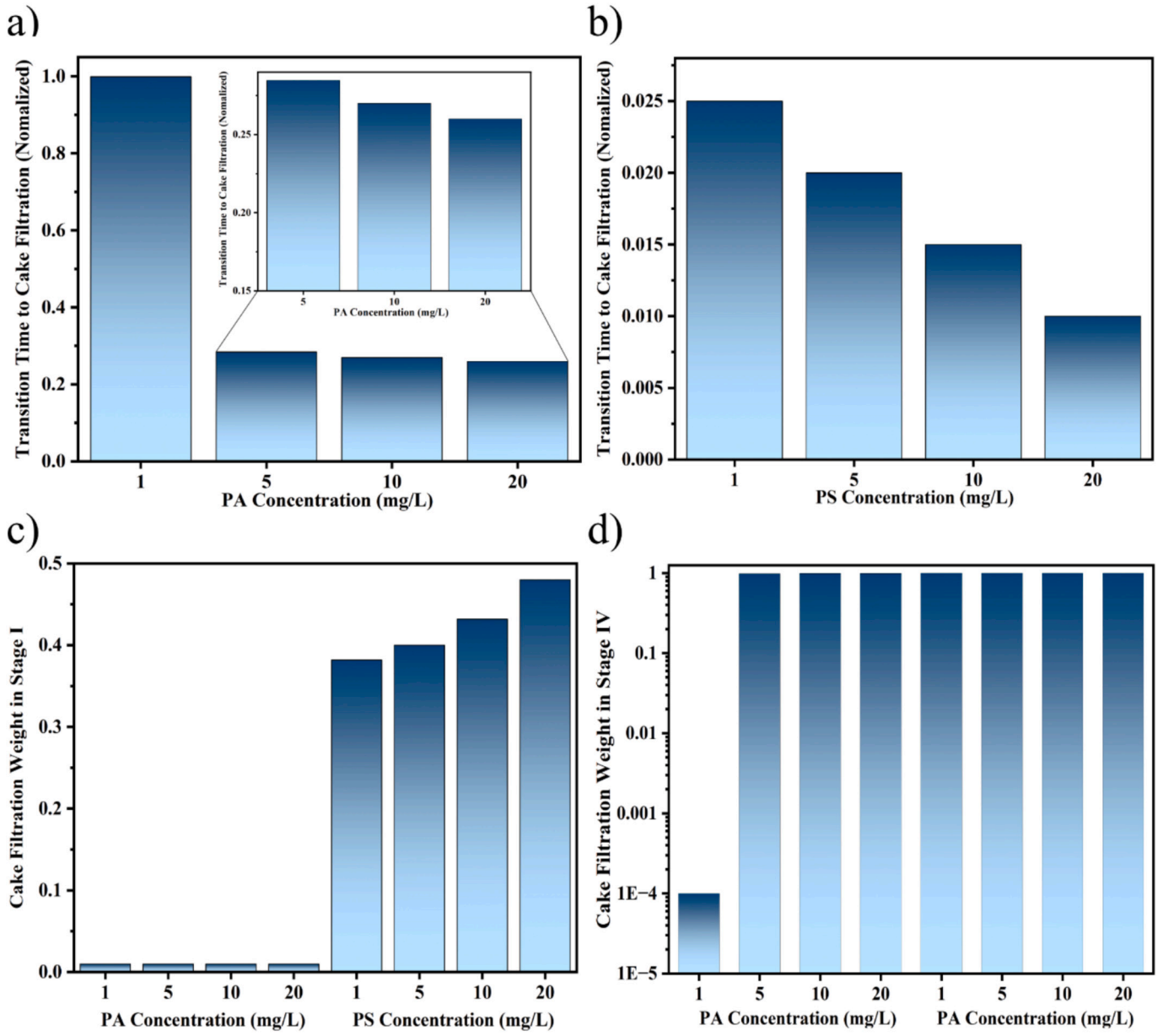

Fig. 6. Influence of particle concentration and particle-to-pore size ratio (d_p/d_m) on fouling behavior of feeds containing PA and PS: (a, b) normalized transition time to cake filtration for PA ($d_p/d_m = 8$) and PS ($d_p/d_m = 22$) at different particle concentrations; and (c, d) fractional contribution of the cake-filtration mechanism in Stages I and IV.

empirical models suffer from non-unique parameter fitting and limited physical interpretability, restricting their utility for practical applications.

The proposed PINN approach overcomes these challenges through three key innovations. First, it introduces smooth, adaptive transitions between fouling stages, achieved using sigmoid-based weighting functions that allow for continuous and dynamic adjustment of each mechanism's contribution as filtration progresses. This formulation captures the true physical continuity of flux decline trends, in contrast to traditional models that rely on rigid or abrupt regime shifts. Second, the PINN employs an adaptive loss-weighting strategy, in which the relative importance of the data loss, physics-based residual loss, and initial condition loss is learned directly during training. This enables the model to balance information from experimental data, initial conditions, and governing physical laws, enhancing stability, robustness, and objectivity in model calibration. Third, the model partitions the flux-time trajectory into distinct stages, each corresponding to different fouling mechanism (s). Within each stage, the PINN quantitatively estimates the relative contributions of the four classical fouling mechanisms. This provides a temporal map of fouling evolution with clear mechanistic interpretation. Compared to classical mechanistic or black-box ML approaches, this framework integrates stage-transition identification and mechanism-resolved weighting within a single physics-informed formulation for membrane-fouling prediction. Evaluation across a diverse dataset encompassing various membrane types and operating conditions demonstrates that the developed PINN achieves high predictive accuracy and low uncertainty while maintaining a direct physical connection to underlying fouling mechanisms.

Overall, this study demonstrates that the PINN framework offers not only high predictive accuracy in predicting flux decline but also

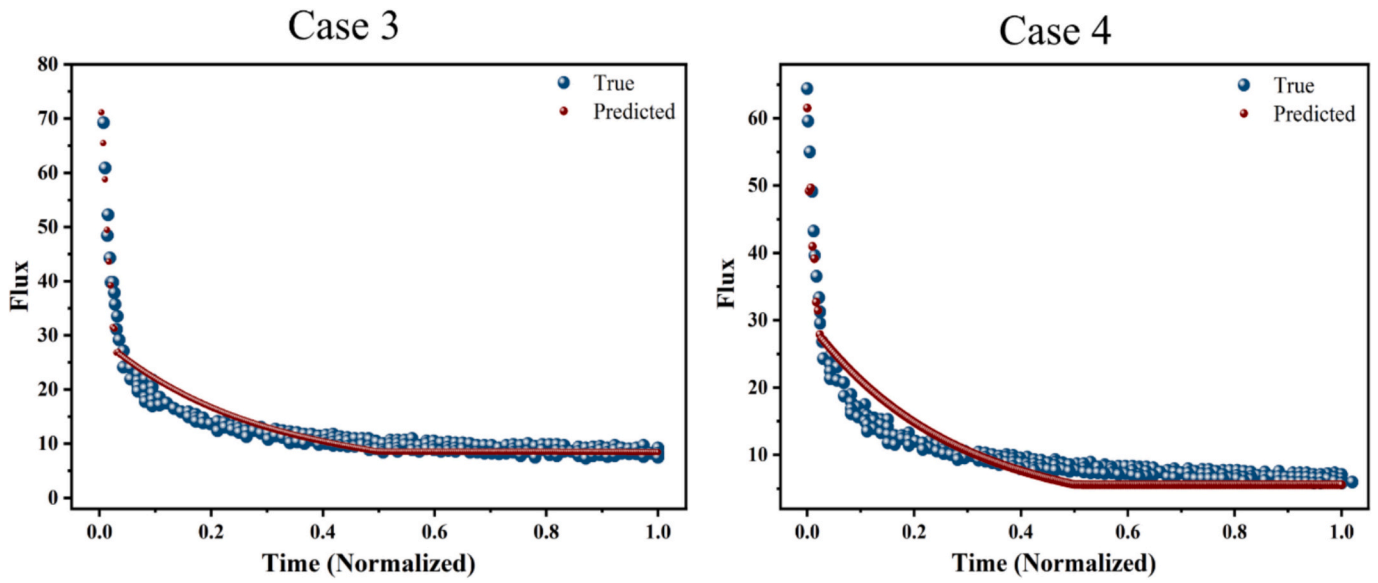

Fig. 7. Comparison of true and predicted flux for Cases 3 and 4 under conditions showing sharp, non-smooth transitions between fouling stages. The abrupt flux decline leads to poor model fitting, demonstrating the limitation of discontinuous regime switching.

enhanced interpretability of the underlying fouling mechanisms. By being able to identify the dominant fouling mechanism at any given time and determine the timing of stage transitions, the model provides physically interpretable insights into membrane filtration. These capabilities have substantial practical implications, for example, operators can schedule cleaning interventions precisely when specific fouling modes dominate, thereby improving maintenance efficiency, extending membrane lifespan, and reducing operational costs. Furthermore, the PINN framework's robust and flexible structure allows straightforward adaptation to diverse membrane-filtration systems and future advancements in process monitoring and control.

Despite these promising results, several limitations should be acknowledged. First, the current validation focuses on lab-scale microfiltration datasets; broader evaluation on long-term, industrial-scale datasets will further establish generalizability. Second, the present formulation is based on the four Hermia mechanisms and thus does not explicitly account for transport and hydrodynamic phenomena such as concentration polarization and shear-dependent effects. Third, transition-time estimation can be sensitive to measurement noise and sensor resolution. Future work can extend the framework to incorporate additional mechanistic constraints and multi-sensor monitoring signals (e.g., TMP, turbidity), enabling real-time soft-sensor prediction and control for fouling mitigation and cleaning optimization.

Declaration of competing interest

The authors declare that they have no known competing financial interests or personal relationships that could have appeared to influence the work reported in this paper.

Acknowledgment

This study was supported by the Chalmers Gender Initiative for Excellence (Genie) and the Swedish Research Council (Grant No. 2025-07412).

Appendix A. Supplementary data

Supplementary data to this article can be found online at https://doi.org/10.1016/j.seppur.2026.137512.

Data availability

Data will be made available on request.

References

[1] A. Alborzi, I.M. Hsieh, D. Reible, M. Malmali, Analysis of fouling mechanism in ultrafiltration of produced water, J. Water Process Eng. 49 (2022), https://doi.org/10.1016/j.jwpe.2022.102978.
[2] H.J. Tanudjaja, A. Anantharaman, A.Q.Q. Ng, Y. Ma, M.B. Tanis-Kanbur, A. L. Zydney, J.W. Chew, A review of membrane fouling by proteins in ultrafiltration and microfiltration, J. Water Process Eng. 50 (2022), https://doi.org/10.1016/j.jwpe.2022.103294.
[3] H.C. Flemming, Biofouling and me: my Stockholm syndrome with biofilms, Water Res. 173 (2020), https://doi.org/10.1016/j.watres.2020.115576.
[4] M. Jafari, M. Vanoppen, J.M.C. van Agtmaal, E.R. Cornelissen, J.S. Vrouwenvelder, A. Verliefde, M.C.M. van Loosdrecht, C. Picioreanu, Cost of fouling in full-scale reverse osmosis and nanofiltration installations in the Netherlands, Desalination 500 (2021), https://doi.org/10.1016/j.desal.2020.114865.
[5] J.W. Chew, J. Kilduff, G. Belfort, The behavior of suspensions and macromolecular solutions in crossflow microfiltration: an update, J. Membr. Sci. 601 (2020), https://doi.org/10.1016/j.memsci.2020.117865.
[6] S. Taghaddosi, A. Akbari, R. Yegani, Preparation, characterization and anti-fouling properties of nanoclays embedded polypropylene mixed matrix membranes, Chem. Eng. Res. Des. 125 (2017) 35–45, https://doi.org/10.1016/j.cherd.2017.06.036.
[7] J. Hermia, Constant pressure blocking filtration laws - application topower-law non-newtonian fluids, Trans Inst Chem Eng V 60 (1982) 183–187.
[8] C.C. Ho, A.L. Zydney, A combined pore blockage and cake filtration model for protein fouling during microfiltration, J. Colloid Interface Sci. 232 (2000) 389–399, https://doi.org/10.1006/jcis.2000.7231.
[9] C. Duclos-Orsello, W. Li, C.C. Ho, A three mechanism model to describe fouling of microfiltration membranes, J Memb Sci 280 (2006) 856–866, https://doi.org/10.1016/j.memsci.2006.03.005.
[10] T.A. Trinh, W. Li, J.W. Chew, Internal fouling during microfiltration with foulants of different surface charges, J. Membr. Sci. 602 (2020), https://doi.org/10.1016/j.memsci.2020.117983.
[11] A.L. Zydney, Development of a new blocking model for membrane fouling based on a composite media model, J. Membrane Sci. Letters 2 (2022), https://doi.org/10.1016/j.memlet.2022.100018.
[12] D.J. Kovacs, Z. Li, B.W. Baetz, Y. Hong, S. Donnaz, X. Zhao, P. Zhou, H. Ding, Q. Dong, Membrane fouling prediction and uncertainty analysis using machine learning: a wastewater treatment plant case study, J Memb Sci 660 (2022) 120817, https://doi.org/10.1016/J.MEMSCI.2022.120817.
[13] T. Wang, Y.Y. Li, Predictive modeling based on artificial neural networks for membrane fouling in a large pilot-scale anaerobic membrane bioreactor for treating real municipal wastewater, Sci. Total Environ. 912 (2024) 169164, https://doi.org/10.1016/J.SCITOTENV.2023.169164.
[14] D. Kim, J.P. Yun, T. Lee, D. Jung, H.I. Won, AI-driven multivariate time series forecasting of transmembrane pressure in ultrafiltration: a stationarity-aware approach, J. Water Process Eng. 77 (2025) 108539, https://doi.org/10.1016/J.JWPE.2025.108539.

[15] Q.F. Liu, S.H. Kim, Evaluation of membrane fouling models based on bench-scale experiments: a comparison between constant flowrate blocking laws and artificial neural network (ANNs) model, J Memb Sci 310 (2008) 393–401, https://doi.org/10.1016/j.memsci.2007.11.020.
[16] Q.F. Liu, S.H. Kim, S. Lee, Prediction of microfiltration membrane fouling using artificial neural network models, Sep. Purif. Technol. 70 (2009) 96–102, https://doi.org/10.1016/j.seppur.2009.08.017.
[17] H.J. Tanudjaja, A.Q.Q. Ng, J.W. Chew, Understanding single-protein fouling in Micro- and ultrafiltration systems via machine-learning-based models, Ind. Eng. Chem. Res. (2023), https://doi.org/10.1021/acs.iecr.3c00275.
[18] B. Li, R. Yue, L. Shen, C. Chen, R. Li, Y. Xu, M. Zhang, H. Hong, H. Lin, A novel method integrating response surface method with artificial neural network to optimize membrane fabrication for wastewater treatment, J. Clean. Prod. 376 (2022), https://doi.org/10.1016/j.jclepro.2022.134236.
[19] B. Li, L. Shen, Y. Zhao, W. Yu, H. Lin, C. Chen, Y. Li, Q. Zeng, Quantification of interfacial interaction related with adhesive membrane fouling by genetic algorithm back propagation (GABP) neural network, J. Colloid Interface Sci. 640 (2023) 110–120, https://doi.org/10.1016/j.jcis.2023.02.030.
[20] L. Sangsuk, K. Jooho, Prediction of Nanofiltration and reverse-osmosis-membrane rejection of organic compounds using random Forest model, J. Environ. Eng. 146 (2020) 04020127, https://doi.org/10.1061/(ASCE)EE.1943-7870.0001806.
[21] H. Mashhadi Meighani, A. Dehghani, F. Rekabdar, M. Hemmati, I. Goodarznia, Artificial intelligence vs. classical approaches: a new look at the prediction of flux decline in wastewater treatment, desalination, Water Treat 51 (2013) 7476–7489, https://doi.org/10.1080/19443994.2013.773861.
[22] S. Safeer, R.P. Pandey, B. Rehman, T. Safdar, I. Ahmad, S.W. Hasan, A. Ullah, A review of artificial intelligence in water purification and wastewater treatment: recent advancements, J. Water Process Eng. 49 (2022), https://doi.org/10.1016/j.jwpe.2022.102974.
[23] X. Meng, F. Wang, S. Meng, R. Wang, Z. Mao, Y. Li, M. Yu, X. Wang, Q. Zhao, L. Yang, Novel surrogates for membrane fouling and the application of support vector machine in analyzing fouling mechanism, Membranes (Basel) 11 (2021), https://doi.org/10.3390/membranes11120990.
[24] M. Raissi, P. Perdikaris, G.E. Karniadakis, Physics-informed neural networks: a deep learning framework for solving forward and inverse problems involving nonlinear partial differential equations, J. Comput. Phys. 378 (2019) 686–707, https://doi.org/10.1016/j.jcp.2018.10.045.
[25] M. Tagliavini, S.A. Snyder, Flux decline prediction in dead-end ultrafiltration combining fluorescence spectroscopy and mechanism-informed machine learning, ACS ES and T Water (2024), https://doi.org/10.1021/acsestwater.4c00473.
[26] S.S. Garakani, J.W. Chew, Development of physics-informed machine-learning models to enhance understanding and prediction of membrane fouling, J Memb Sci 728 (2025), https://doi.org/10.1016/j.memsci.2025.124133.
[27] L. Palacio, C.C. Ho, A.L. Zydney, Application of a pore-blockage - cake-filtration model to protein fouling during microfiltration, Biotechnol. Bioeng. 79 (2002) 260–270, https://doi.org/10.1002/bit.10283.
[28] A.D. Marshall, P.A. Munro2, G. Trsgkdh3, The effect of protein fouling in microfiltration and ultrafiltration on permeate flux, protein retention and selectivity : A literature review, 1993.
[29] A. Kendall, Y. Gal, What uncertainties do we need in bayesian deep learning for computer vision? NIPS'17: Proceedings of the 31st International Conference on Neural Information Processing Systems (2017) 5580-5590, doi: 10.5555/3295222.3295309.
[30] M. Cifuentes-Cabezas, J.L. Bohórquez-Zurita, S. Gil-Herrero, M.C. Vincent-Vela, J. A. Mendoza-Roca, S. Álvarez-Blanco, Deep study on fouling modelling of ultrafiltration membranes used for OMW treatment: comparison between semi-empirical models, response surface, and artificial neural networks, Food Bioprocess Technol. 16 (2023) 2126–2146, https://doi.org/10.1007/s11947-023-03033-0.
[31] P.H. Hermans, H.L. Bredée, Zur Kenntnis der Filtrationsgesetze, Recl. Trav. Chim. Pays-Bas 54 (1935) 680–700, https://doi.org/10.1002/recl.19350540902.
[32] J. Hermia, Constant Pressure Blocking Filtration Laws - Application to Power-Law Non-newtonian Fluids. https://api.semanticscholar.org/CorpusID:61145250, 1982.
[33] M. Bagheri, A. Akbari, S.A. Mirbagheri, Advanced control of membrane fouling in filtration systems using artificial intelligence and machine learning techniques: a critical review, Process Saf. Environ. Prot. 123 (2019) 229–252, https://doi.org/10.1016/j.psep.2019.01.013.
[34] B. Ghalami Choobar, M.A. Alaei Shahmirzadi, A. Kargari, M. Manouchehri, Fouling mechanism identification and analysis in microfiltration of laundry wastewater, J. Environ. Chem. Eng. 7 (2019), https://doi.org/10.1016/j.jece.2019.103030.
[35] A.R.P. Pizzichetti, C. Pablos, C. Álvarez-Fernández, K. Reynolds, S. Stanley, J. Marugán, Kinetic and mechanistic analysis of membrane fouling in microplastics removal from water by dead-end microfiltration, J. Environ. Chem. Eng. 11 (2023), https://doi.org/10.1016/j.jece.2023.109338.
[36] B.D. Cho, A.G. Fane, Fouling Transients in Nominally Sub-Critical Flux Operation of a Membrane Bioreactor, 2002.
[37] S. Ognier, C. Wisniewski, A. Grasmick, Membrane bioreactor fouling in sub-critical filtration conditions: a local critical flux concept, J Memb Sci 229 (2004) 171–177, https://doi.org/10.1016/j.memsci.2003.10.026.